AIP | Journal of Applied Physics

Investigations of the polymer alignment, the nonradiative resonant energy transfer, and the photovoltaic response of poly(3-hexylthiophene)/TiO2 hybrid solar cells

Young Ran Park, You-Jin Lee, Chang-Jae Yu, and Jae-Hoon Kim

Citation: J. Appl. Phys. **108**, 044508 (2010); doi: 10.1063/1.3459889
View online: http://dx.doi.org/10.1063/1.3459889
View Table of Contents: http://jap.aip.org/resource/1/JAPIAU/v108/i4
Published by the American Institute of Physics.

Investigations of the polymer alignment, the nonradiative resonant energy transfer, and the photovoltaic response of poly(3-hexylthiophene)/TiO_2 hybrid solar cells

Young Ran Park,[1] You-Jin Lee,[2] Chang-Jae Yu,[2] and Jae-Hoon Kim[2]
[1]*Department of Electronics and Computer Engineering, Research Institute of Information Display, Hanyang University, Seoul 133-791, Republic of Korea*
[2]*Department of Information Display Engineering, Department of Electronics and Computer Engineering, Hanyang University, Seoul 133-791, Republic of Korea*

(Received 13 January 2010; accepted 4 June 2010; published online 27 August 2010)

We report the effects of annealing on the performance of hybrid photovoltaic (PV) cells containing poly(3-hexylthiophene) (P3HT) coated onto TiO_2/Sn doped In_2O_3 (ITO) and ITO substrates. In the optimized device, which exhibits a higher efficiency, the backbone axes of the P3HT chains were found to lie within the substrate plane, their conjugated planes are slightly tilted, and their side chains are substantially tilted. The carboxylate group is attached via bidentate or bridging coordination to the TiO_2 surface and enables photoinduced charge transfer between TiO_2 and P3HT. The observed large quenching (with excitation at 488 nm) and enhanced emission (with excitation at 325 nm) indicates that efficient Förster resonance energy transfer occurs between TiO_2 and P3HT. Thus, the main influences on the high efficiency of the hybrid PV cells are the photon-mediated electronic transition and the photoinduced charge transfer. © *2010 American Institute of Physics*. [doi:10.1063/1.3459889]

I. INTRODUCTION

During the past decade, there has been growing interest in the development of cheap hybrid organic/inorganic photovoltaic (PV) cells because of their potential applications in new types of optoelectronic devices.[1–7] In comparison to polymer solar cells, these hybrid devices exhibit superior charge separation efficiency, balanced carrier-transport properties, and solar absorption, all of which lead to enhanced power conversion efficiency. Although in contrast to CdSe nanostructures, TiO_2 does not absorb visible light, it does have some potential advantages over CdSe and PCBM as an electron-accepting material. In a typical hybrid material, Wannier excitons are formed in the inorganic component and Frenkel excitons are formed in the organic component. Those excitons that are produced within the interface between the organic and the inorganic semiconductors can contribute to the PV effect, so there is a need to improve the transparency of exciton interfaces. Excitons in the donor material transfer their energy to the closest acceptor materials via the donor acceptor interface. Fluorescence (Förster) resonance energy transfer (FRET) (Refs. 8 and 9) is energy transfer between two fluorescent materials through long range dipole–dipole interactions (Wannier and Frenkel excitons). Blumstengel *et al.*[10] and Itskos *et al.*[11] recently reported FRET interactions between the Wannier excitons in inorganic quantum layers and the Frenkel excitons in organic layers.[10,11] They demonstrated that efficient dipole–dipole energy transfer between Wannier and Frenkel excitons occurs in hybrid materials. In solar cells, excitons are generated by light absorption and their subsequent dissociation results in separated electron–hole pairs. Exciton dissociation [photoinduced charge transfer (CT)] results in the quenching of the polymer photoluminescence (PL).

Our focus in this study was to investigate the energy conversion efficiencies in organic-inorganic PV devices consisting of a TiO_2 layer as the main exciton dissociation site and poly(3-hexylthiophene) (P3HT). We carried out measurements in which we modified the polymer morphology though postannealing; these measurements were designed to systematically probe the effects of internal resistance, polymer hole mobility, and the surface area of the exciton dissociation site on the charge transport properties of the hybrid PVs. Hybrid solar cells with improved performance are obtained by using TiO_2, which results in an extended pathway interfacial area for charge separation and a straight pathway for electron transport to the Sn doped In_2O_3 (ITO) electrode.

II. EXPERIMENTAL DETAILS

A. Film preparation

Anatase TiO_2 thin films were deposited on ITO (120 nm) electrode coated glass substrates by using a sol-gel method with a spin-coating process.[12] The precursor solution was prepared by dissolving titanium butoxide, $Ti[O(CH_2)_3CH_3]_4$, in the solvent at 70 °C. When 2-methoxyethanol was employed as the solvent, the resulting films were found to have an anatase structure. The precursor solution was stirred at 70 °C for 2 h to increase its homogeneity. Prior to the deposition of the films, the substrates were cleaned with acetone followed by methanol in an ultrasonic bath. The substrates were spin-coated with the precursor solution at 3000 rpm for 20 s to prepare the precursor films, and then preheated in air at 120 °C for 5 min after each deposition in order to remove

[a]Electronic mail: jhoon@hanyang.ac.kr.

organic substances. This process was repeated to increase the film thickness. After the spin-coating process, the precursor films were annealed at 400 °C for 2 h in a box furnace. The thicknesses of the deposited films were determined with field emission scanning electron microscopy (FESEM) and found to be in the range 170 ± 10 nm.

Regioregular P3HT (regioregularity=92%, Mn=26 700, and PDI=1.78) was purchased from Rieke Metals Inc.. All of the polymer thin films were prepared on ITO and TiO_2/ITO coated glass by spin coating. The P3HT polymers were dissolved in chloroform ($CHCl_3$) and spin-coated with a solution concentration of 3.0 mg/ml at 800 rpm for 40 s to prepare precursor films that were then preheated in air at 100 °C for 2 min. The thickness was controlled to approximately 100 nm by varying the solution concentration and the conditions of the spin-coating process. We also varied the postannealing conditions after film deposition, with the aim of investigating the effects on recrystallization and charge transport in the P3HT films. Of the three P3HT films, the one with the TiO_2/ITO coated substrate was maintained in air in a box furnace at 150 °C for 1 h. The films with TiO_2/ITO and ITO coated substrates were annealed at 240 °C (above the melting temperature of P3HT) for 1 h in a N_2 atmosphere at a pressure of about 100 mTorr in a quartz tube furnace and then slowly cooled to room temperature. Finally, the Au top electrode was thermally evaporated through a shadow mask. A conventional ITO bottom electrode film with a thickness of approximately 120 nm was prepared at a low temperature on a glass substrate, and found to have a polycrystalline cubic structure. The active area of each device defined by the shadow mask was 0.04 cm^2.

B. Film characterization

In the structure analysis, three different kinds of x-ray diffraction (XRD) investigations were performed: normal XRD, high resolution grazing incidence XRD (HRGIXD), and pole figure measurements with focused Cu $K\alpha$ radiation. The out-of-plane/in-plane alignments of the crystallites were determined with the pole figure measurements. The angle of incidence was adjusted to be close to the critical angle for total reflection against the substrate. The optical absorbances of the TiO_2 and P3HT thin films were recorded with an ultraviolet-visible spectrometer over the wavelength range 300–900 nm. The surface roughness, morphology, and thickness of each of the deposited TiO_2 and P3HT films were investigated with atomic force microscopy (AFM) and FESEM. Photoluminescence (PL) measurements were performed under ambient air conditions by using a Hamamatsu photonic multichannel analyzer. He-Cd and Ar lasers were used for the excitations at 325 nm and 488 nm, respectively. The spectrometer was calibrated with an atomic emission from a neon lamp, and was tested with silicon lines before each spectrum was obtained. The micro-Raman measurements were performed in the backscattering geometry. The 514 nm line of an Ar laser was focused to a beam with a diameter of approximately 10 μm, and the incident light was scanned along the x and y directions of the samples. The scattered light from each sample was passed through a broadband polarization scrambler to eliminate polarization effects in the monochromator. Reflection-type Fourier transform infrared (FT-IR) spectroscopy was carried out to examine the changes in the hydrogen bonding configurations. During the measurements, all films were kept in a chamber under a N_2 atmosphere (30 mTorr). The surfaces of the films were irradiated with unpolarized IR light, and the measurements were obtained at an angle of 64° from the plane of incidence. Two thousand scans were obtained over the wave number range 1400–4000 cm^{-1} with a resolution of 0.1 cm^{-1}. Fourier transform (FT)-Raman spectra were obtained using a Bruker Vertex 70 spectrometer. An Nd-YAG laser was used to produce excitation energy at a wavelength of 1064 nm and resolution was set at 0.15 cm^{-1}.

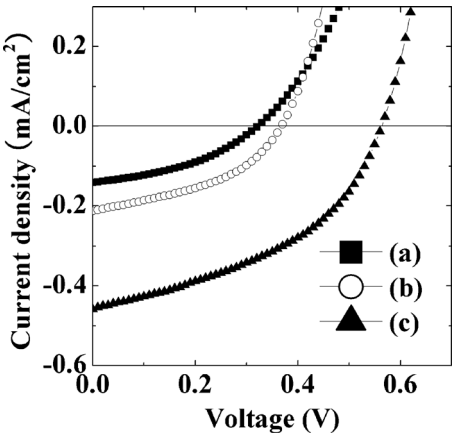

FIG. 1. Current density as a function of applied voltage for the ITO/TiO_2/P3HT/Au devices with various annealing conditions: (a) with TiO_2 in air; (b) without TiO_2 in N_2; (c) with TiO_2 in N_2. The incident light intensity was 100 mW/cm^2 (1 sun).

C. Device characterization

Electron transport in the ITO/TiO_2/P3HT/Au devices was investigated by examining the current density versus voltage (J-V) curves, which were obtained with a computer-controlled HP 4155C source-measure unit by sourcing voltages across the ITO (cathode) and Au (anode) electrodes and measuring the resulting current density. The photocurrent was measured under a solar illumination of AM (air mass) 1.5G (global) at 100 mW/cm^2 (1 sun), as supplied by a Newport 150 W solar simulator, and the light intensity for the AM 1.5G spectrum was monitored with a calibrated silicon photodiode. All measurements were performed in the ambient atmosphere at room temperature.

III. RESULTS AND DISCUSSION

Figure 1(a) shows the variations in the current density with the applied voltage (J-V) for the hybrid PVs fabricated with a TiO_2 layer. The P3HT film of (a) was annealed in air for 1 h (with TiO_2 in air). Figures 1(b) and 1(c) show the J-V curves of hybrid PVs fabricated without and with a TiO_2 layer, respectively. The P3HT films of (b) and (c) were annealed in a N_2 atmosphere (100 mTorr) in a quartz tube furnace for 1 h. For the ITO/TiO_2/P3HT/Au devices, the open-circuit voltage V_{oc} under illumination was determined

TABLE I. Comparison of the PV parameters and rms roughnesses of the P3HT-based and TiO_2/P3HT-based devices under 100 mW/cm^2.

	ITO/TiO_2/P3HT/Au	ITO/P3HT/Au	ITO/TiO_2/P3HT/Au
Annealed conditions of the P3HT film	In air in a box furnace at 150 °C for 1 h	In a N_2 atmosphere with a pressure of approximately 100 mTorr in a quartz tube furnace at 240 °C for 1 h	
J_{sc} (mA/cm^2)	0.141	0.212	0.460
V_{oc} (V)	0.325	0.370	0.57
P_{max} (mW/cm^2)	0.02	0.03	0.11
Fill factor (*FF*)	0.395	0.425	0.428
Efficiency (%)	0.02	0.03	0.11
R_s (Ω cm^2)	121.6	74.5	61.6
rms roughness (nm)	9.11	3.82	4.72

from the difference between the quasi-Fermi energy level of TiO_2 (4.2 eV) and the work function of the Au electrode or the highest occupied molecular orbital (HOMO) level of P3HT. In our system, the Au electrode (work function 5.1 eV) forms a nearly non-Ohmic contact with the HOMO of P3HT (5.2 eV). Exciton dissociation occurs at the TiO_2-polymer interface, with the transfer of electrons to the TiO_2 the main process of charge collection. Moreover, TiO_2 serves as an effective hole blocker.

Table I summarizes the effects of the postannealing of P3HT on the PV parameters and rms roughnesses of the films. The main overall effects of postannealing are the improvements in all the parameters [J_{sc}, V_{oc}, and fill factor (*FF*)] relevant to the energy conversion efficiency. Device performance was found to improve with postannealing in a N_2 atmosphere, and the devices that had been slow-cooled from the melt at 240 °C were found to exhibit a V_{oc} of 0.57 V, a J_{sc} of 0.46 mA/cm^2, a *FF* of 0.428, and a power conversion efficiency of 0.11%. This improved charge transport is consistent with the increase in *FF* upon postannealing. Note that in spite of its low open-circuit voltage, the ITO/P3HT/Au solar cell exhibits a remarkably high *FF* of 0.425, which is similar to that of the ITO/TiO_2/P3HT/Au solar cell (*FF* of 0.428) obtained under the same N_2 atmosphere annealing conditions. A similar *FF* arises in fabricated solar cells because of a similar leakage current or shunt resistance. In general, an improved shunt resistance or leakage current is due to the reduction of defects such as dislocations in the bulk portion or at the interface of the heterojunctions. These findings are in good agreement with the results of the HRGIXD and PL measurements. In particular, the series resistances [$R_s \sim (J/V)^{-1}$] of the devices were estimated from the inverse slope at the forward bias voltage above V_{oc}, as shown in Fig. 2. The performance of the device stored in air increases due to both an increase in the shunt resistance and a decrease in the series resistance, which results in increased *FF* and V_{oc} values. The performance of device (a) was found to be rather poor: $FF=0.395$ and $R_s=121.6\ \Omega\ \text{cm}^{-1}$.

These PV parameters were considerably improved after postannealing in a N_2 atmosphere ($FF=0.428$ and $R_s=61.6\ \Omega\ \text{cm}^{-1}$). Therefore, postannealing under N_2 conditions improves the light harvest in the active layer and hinders the formation of shunt paths in the donor/acceptor structure when compared to annealing under air conditions.

Figure 3 shows the out-of-plane ($\psi=0°$) and from the out-of-plane ($\psi=0°$) to the in-plane ($\psi=90°$) XRD patterns of the θ-2ω scans obtained for grazing incidence with normal XRD (GIXD) and HRGIXD. Figure 3(a) shows the (100) reflection and its higher order reflections, which correspond to the side-chain lamellar stacking distance. The presence of only (l00) reflections indicates that the main chains (the P3HT backbones) have a tendency to orient parallel to the TiO_2 and ITO surfaces. In the in-plane ($\psi=90°$) θ-2ω scans, the reciprocal space is probed in the z direction (q_z, where **q** is the scattering vector and z is perpendicular to the sample surface), and therefore planes parallel to the surface can be investigated with these measurements. The transformation between the measured angles and reciprocal space was performed by using the following expression, where λ is the wavelength and 2θ is the diffraction angle:

$$q = \frac{2\pi}{d} = \frac{4\pi}{\lambda}\sin\left(\frac{2\theta}{2}\right). \quad (1)$$

In Figs. 3(b)–3(d), only meridional (100), (200), and (300) reflections can be distinguished at $q=0.37$ Å^{-1} (d

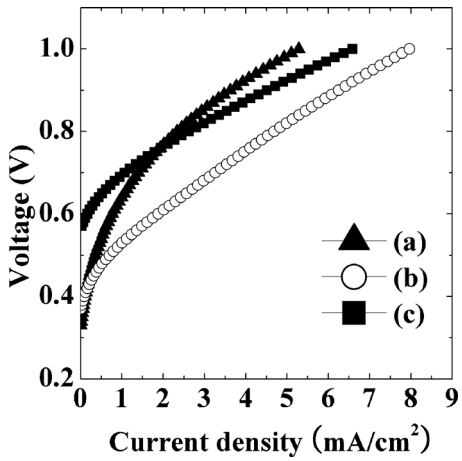

FIG. 2. The forward bias voltage above V_{oc} as a function of the current density for the ITO/TiO_2/P3HT/Au devices with various annealing conditions: (a) with TiO_2 in air; (b) without TiO_2 in N_2; (c) with TiO_2 in N_2. The incident light intensity was 100 mW/cm^2 (1 sun).

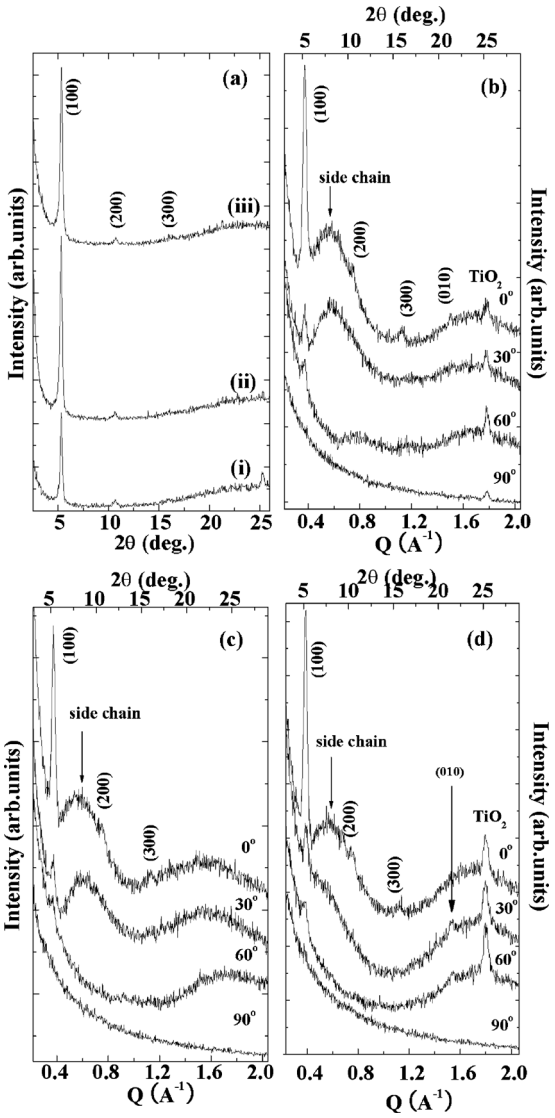

FIG. 3. XRD spectra for the directionally regioregular crystallized P3HT layers in the PV cells. (a) Out-of-plane (ψ=0°) grazing incidence angle at normal XRD intensities as a function of the scattering angle (2θ): (i) with TiO_2 in N_2; (ii) with TiO_2 in air; (iii) without TiO_2 in N_2. [(b)–(d)] From the out-of-plane (ψ=0°) to the in-plane (ψ=90°) grazing incidence angle at high resolution XRD intensities as a function of the scattering angle (2θ) and scattering vector (**q**): (b) without TiO_2 in N_2; (c) with TiO_2 in air; (d) with TiO_2 in N_2.

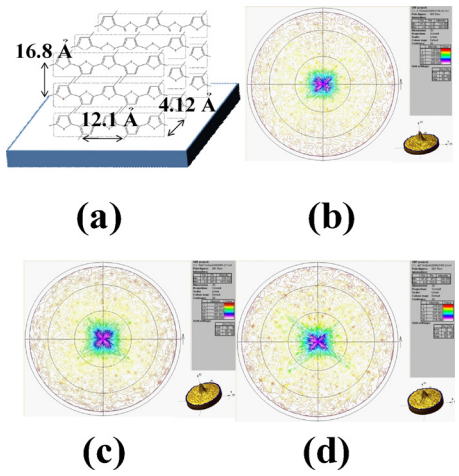

FIG. 4. (Color online) (a) Schematic representation of the regioregular-P3HT $\pi-\pi$ stacking structure. X-ray pole figures {001} for P3HT (100) on TiO_2 and/or ITO films showing c-axis oriented backbone-stacking growth with tilting angle (ψ): (b) without TiO_2 in N_2; (c) with TiO_2 in air; (d) with TiO_2 in N_2.

=16.80 Å), q=0.74 $Å^{-1}$ (d=8.48 Å), and q=1.11 $Å^{-1}$ (d =5.65 Å), which correspond to the stacking periodicity parallel to the long axis of the alkyl side chains. The plane ψ =30° and 60° results in a Bragg reflection at q=1.52 $Å^{-1}$ (d=4.12 Å), which is assigned to the (010) line corresponding to the $\pi-\pi$ (inter-chain) stacking of the P3HT chains. The low intensity of this (010) reflection peak is indicative of defects in the close packing of the chains in this direction. Note that this reflection is superimposed on a broad halo originating from the glass substrate. The presence of the reflection corresponding to the (100) plane in both diffraction patterns seems to indicate that this plane, although perpendicular to the long axis, can adopt different orientations with respect to rotation around this axis. It might originate from a population of nanorods with a 90° rotation around their long axis with respect to the other ones present in the layer [see Figs. 4(a)–4(d)]. Note that for these rods the (200) line is not visible, which suggests there is more extended disorder of the alkyl side chains in these nanorods. Orientations determined with near edge x-ray absorption fine structure (NEXAFS) or other polarized light spectroscopies are not often interpreted as explicit molecular orientations within crystals because they are the azimuthal averages of unknown orientation distributions.[13] For P3HT however, the pole figure measurements and GIXD indicate the presence of a comprehensive crystallinity of a single type. It is thus reasonable to assume a tight and monomode orientation distribution of the conjugated planes. DeLongchamp *et al.*[13] recently reported the dependence of the total energy on the tilt of the conjugated plane: the energy has a local maximum for a tilt of 0° and a minimum for a tilt of 27.5°. The tilting angle (α) is defined as the angle between the conjugated thiophene-ring plane (backbone) and the a-axis (the normal direction of the substrate surface), as shown in Fig. 4(a). This result was obtained with CH_3 side groups, and it is likely that longer side chains would substantially shift the tilt landscape. Thus, the conjugated-plane tilt contributes strongly to the energetic stability of the crystal structure.

By comparing the experimental (100) intensities with the variations in the XRD results, the average molecular orientations of the polymer backbones can be estimated. In the HRGIXD measurements, the angle ψ (from 0° to 90°) corresponds to the tilt angle (α) of the conjugated-plane orientation. Therefore, the HRGIXD measurements can be assigned to the tilt angle for the conjugated-plane orientation. As previously mentioned in the discussion of the HRGIXD results, the P3HT in Fig. 3(b) has more edge-on character than the P3HT in Fig. 3(d), although all the samples have a tilted conformation, whereas the P3HT in Fig. 3(c) has more disordered character. Thus, a slight "slip" of the face-on/edge-on structure is evident from the different intensity distributions of the (100) reflections corresponding to the main chain (backbones) stacking (16.80 Å, a-axis) and the (010) reflections corresponding to the $\pi-\pi$ interchain stacking

(4.12 Å, b-axis) in the variation in the geometric modes. The overlap of the π electronic wave function within the lamellae planes should result in increased intralayer mobility in the P3HT films. On the other hand, π electronic states distributed outside the polymer surface can overlap with the π electronic wave functions of an overlayer molecular material, which can provide efficient CT in the heterojunction structures used in polymer devices.

The persistence length of regiorandom P3HT has been reported to be 2.1 nm,[14] but since regioregularity defects cause twists in polymer chains, the persistence length of highly regioregular P3HT should be significantly longer. The high molecular weight polymer molecules are approximately 80 nm long. The molecules are expected to have multiple bends along their length. We believe that P3HT forms small ordered areas separated by disordered regions and that long chains connect the ordered areas and prevent charge carriers from being trapped by the disordered boundary regions by creating a continuous pathway through the film. The PV cells with TiO_2 annealed in a N_2 atmosphere exhibit a higher efficiency when no alkyl chain stacking is observed [Fig. 3(d)]. Hole delocalization and interchain interactions ($\pi-\pi$ stacking) can benefit carrier transport in conjugated regioregular P3HT thin films.[15] However, the presence of insulating side chains in the surface region can be detrimental to the CT between the polymer backbone and the overlayer molecules.

Alkyl-substituted P3HT has a backbone of sequentially bonded thiophene rings with linear alkane chains attached to their sides. In thin films, they self-assemble into lamellae; a layer-packing motif where planar backbones π stack in lamellae vertically segregated from lamellae of side chains has been developed by comparing typical unit-cell dimensions to molecular dimensions,[16–18] and is generally accepted. Two critical but poorly characterized aspects of the crystal structure are the conjugated-plane tilt and the alkane side-chain configuration. In the lamellar motif, the conjugated planes must be roughly vertical (orthogonal to the lamella) so that they can π stack face-to-face within a quasi-two-dimensional sheet. However, a variety of conjugated-plane tilts and many possible side-chain configurations distinguished by varying the tilt and the degree of interdigitation are consistent with this layer-packing motif and the available diffraction data. The carrier transport depends critically on the intermolecular overlap of the carrier band orbitals, which is controlled by the conjugated-plane spacing and tilt.

In recent calculations for two-dimensional polythiophene sheets, significant rotation of the polymer backbone was predicted to be energetically favorable. This tilt is important because it governs the interactions between neighboring chains, and therefore has a significant effect on the band structure and the optical properties of the material. The present study performed structural investigations of P3HT layers grown epitaxially on TiO_2(200) and ITO(440) crystal surfaces. The crystal alignment and the epitaxial relationships between the substrates and thin-film crystals were determined experimentally by using XRD techniques.

Figure 4(a) shows a schematic diagram of the molecular structure of the P3HT thin films on the glass substrate, as determined from the XRD data results. This model was confirmed by the presence of a symmetric lattice plane, as observed in the multiple reflections (00l), $l=1-3$.

Figures 4(b)–4(d) show the x-ray pole figures {001} for P3HT (100) on TiO_2 and ITO films, which indicate the presence of c-axis oriented backbone-stacking growth with a tilting angle. The pole figures were determined for steps of ψ and φ, where ψ is the polar (or radial) angle and φ is the azimuthal angle (in-plane rotation). Since each pole figure is measured at a constant diffraction angle (constant $|\mathbf{q}|$), it gives the spatial distribution of a certain net plane. The plane normals are called poles, and therefore peaks in pole figures are known as areas of enhanced pole density. For a set of pole figures performed for different net planes, the complete orientation distribution of the crystallites and their orientation relative to the substrate (epitaxial relationship) can be determined unambiguously. For all the PV cells, the pole figure {001} of P3HT (100) has a diagonal shape over the polar angle range 0°–10°. The peak for (440) ITO ($2\theta=50.65°$) interferes with that of (200) TiO_2 ($2\theta=48.07°$). The pole figure shown in Fig. 4 also contains four peak position directions. These peak positions are due to the TiO_2 and ITO films. The backbone axes are within the substrate plane, the conjugated planes are slightly tilted, and the side chains are substantially tilted. The displacement of the side chains from the conjugated plane is speculative but consistent with their known tilt. This effect could be due to the inferior crystal quality that results from a relaxation of the P3HT layer, which generates dislocations (increasing leakage current and recombination).

The morphology and microstructure of polymeric semiconductors and especially of semicrystalline polymers play very important roles in the charge transport in these devices. In particular, defects, grain boundaries, and disordered regions contribute to localize states. Figure 5 shows AFM images of P3HT surfaces in following PV cells: (a) without TiO_2 in N_2, (b) with TiO_2 in air, and (c) with TiO_2 in N_2. In Table I, the P3HT of Fig. 5(c) has a smooth surface with a rms roughness (R_{rms}) of 4.72 nm, whereas the P3HT surface in Fig. 5(b) is rougher ($R_{rms}=9.11$ nm). This result is consistent with that of Fig. 5(a), which was prepared under similar conditions and has a rather smoother surface ($R_{rms}=3.82$ nm). In particular, we have demonstrated the correlation between *FF* and surface roughness at the charge separation interface.

A P3HT [Fig. 6(c)] film deposited uniformly onto an ITO [Fig. 6(a)] substrate (120 nm) was coated with a TiO_2 [Fig. 6(b)] film. Figure 6 shows a cross-section and a top-view of the resulting TiO_2/P3HT hybrid layers under the FESEM. The hybrid film is uniform over the entire substrate. The cross-section clearly shows that P3HT interpenetrates inside the TiO_2 grain and occupies nearly the entire space surrounding the grains. The P3HT deposit above the TiO_2 film forms a solid film approximately 50 nm thick that can potentially prevent electron back transfer and reduce dark current. Our structural observations, including with XRD and AFM, show that the ordered P3HT lamella is nanocrystalline, and that the size of the ordered regions is 10 nm.[18–20] In Fig. 6(c), the FESEM results show that the average crystal-

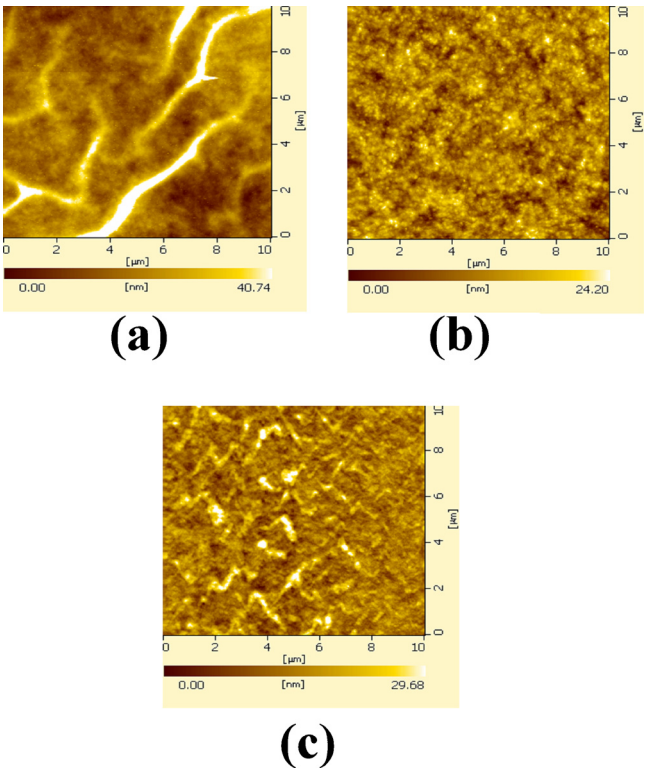

FIG. 5. (Color online) AFM images of the P3HT layers in the PV cells: (a) without TiO_2 in N_2; (b) with TiO_2 in air; (c) with TiO_2 in N_2. The dimensions of the images are 10×10 μm^2.

lite size is approximately 20 nm, and that there are substantial regions of disordered material. Other growth conditions result in a more needlelike microstructure.[21]

It is well known that TiO_2 has three natural phases: anatase, rutile, and brookite.[22] Anatase is tetragonal (D19 4h) with two formula units per unit cell and six Raman active modes ($A_{1g}+2B_{1g}+3E_g$). The Raman spectrum in Fig. 7(a) shows that the film is composed of the anatase phase. Five clear and strong peaks at 144, 194, 395, 518, and 638 cm^{-1} arise from the optical vibration modes Eg($\nu6$), Eg($\nu5$), B1g($\nu4$), A1g+B1g($\nu2+\nu3$), and Eg($\nu1$).[23] Figure 7 provides further information about the interface between P3HT and TiO_2 coated on the ITO electrode, respectively. Small differences can be found between the Raman lines of P3HT on the TiO_2 and ITO substrates. The band assignments of the Raman spectra of polythiophene have been reported in detail.[27] The characteristic peaks of C—S—C ring deformation (672 and 726 cm^{-1}), C_β—H symmetric in-plane bending (1090 cm^{-1}), C_α—$C_{\alpha'}$ inter-ring stretching (1200 cm^{-1}), C_β—$C_{\beta'}$ ring stretching (1379 cm^{-1}), C_α=C_β ring stretching (1445 cm^{-1}), and C_α=C_β stretching (anti) (1506 cm^{-1}), are all present in both spectra. As can be seen in Fig. 7, the most intense band of the spectrum obtained by excitation at 514 nm appears at approximately 1445 cm^{-1}, which is assigned to the total symmetric in-phase vibration of the thiophene rings spreading over the whole polymer chain. This band is associated with the conjugated polymer segments in a neutral state. The relative intensities of the other characteristic peaks were normalized, with the highest peak in both spectra at 1445 cm^{-1}. The

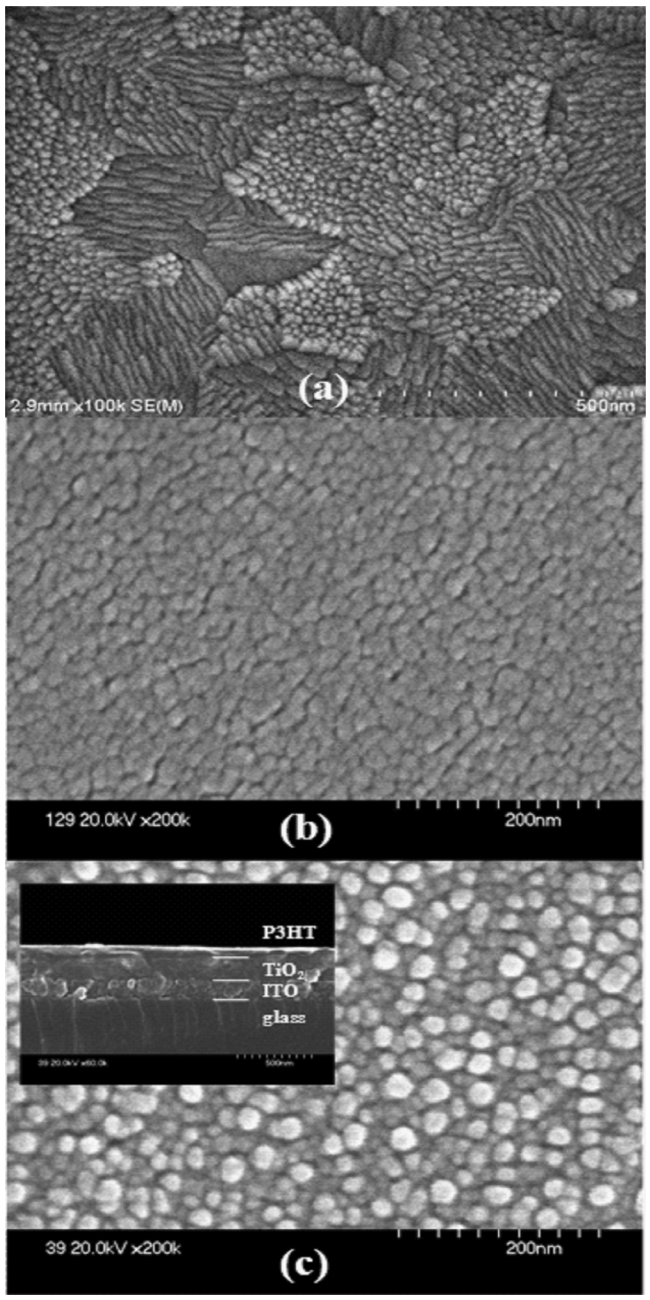

FIG. 6. FESEM images for the ITO/TiO_2/P3HT/Au devices: (a) ITO; (b) pure TiO_2; (c) P3HT (annealed at 240 °C for 1 h under a N_2 atmosphere at a pressure of approximately 100 mTorr in the quartz tube furnace). The inset in (c) shows cross-section images of the PV cells.

Raman bands are related to oxidized species such as radical cations (polaron), dications (dipolaron), and the kinks are of increased intensity.[24] In the inset in Fig. 7, the band at 1420 cm^{-1} (Q_1) is attributed to the symmetric stretching mode (C=C) of radical cations and the kink bands (1455 cm^{-1}, D bands) are associated with distorted parts of polymer chains.[24] A few papers have discussed the changes in the chain structures of conducting polymers during heating and cooling processes, and have reported that the thermal stabilities and conformational transition behaviors of oxidized (doped) and neutral (undoped) conducting polymers are different. It is believed that such changes in chain structure are due to extrinsic defects, such as oxygen. During the

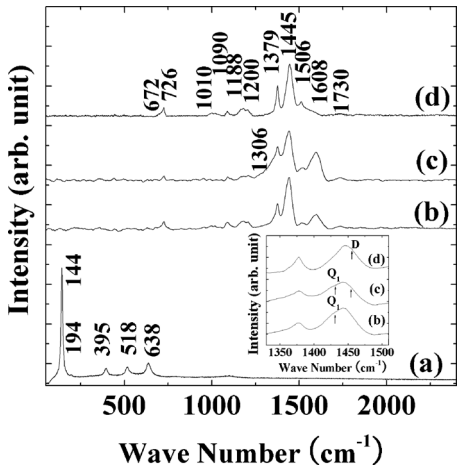

FIG. 7. Micro-Raman spectra of the TiO_2 films and PV cells obtained by using Ar laser excitation at 514 nm: (a) pure TiO_2; (b) with TiO_2 in air; (c) without TiO_2 in N_2; (d) with TiO_2 in N_2.

postannealing of the TiO_2/P3HT layer in air, oxygen attacks and is diffused into P3HT mainly through the first C—H bond of the alkyl chains; a series of steps then leads to chain breakage. In addition, the significant oxidation effects in P3HT can be explained in terms of the hole doping of the donor levels, which can occur even after postannealing. It is reasonable to conclude that the oxidized species in P3HT are mainly present as radical cations. It is thought that dications ($1400\ cm^{-1}, Q_2$) are not formed in P3HT. Therefore, these experimental results demonstrate that single charges are stored in polaron states and that two charges are expected to be stored in two independent polar states rather than in a single bipolaron for long polymer chains. The inset in Fig. 7(b) shows a small Q_1 mode, even though P3HT was annealed at 240 °C for 1 h in a N_2 atmosphere with a pressure of approximately 100 mTorr. The ITO electrode was deposited by sputtering at a substrate temperature of 200 °C, which is lower than the postannealing temperature of P3HT [see Fig. 6(a) and Ref. 25]. Thus the oxygen in the ITO electrode diffuses into P3HT during the postannealing of the P3HT/TiO_2 layer, which induces oxidation effects in P3HT.

A very weak C═O stretching vibration mode is evident at $1730\ cm^{-1}$. The presence of this mode can be explained in terms of the contributions of nonadsorbed molecules and free ligands to the spectrum. Thus, the relatively strong band at $1730\ cm^{-1}$ in Figs. 7(b) and 7(c) indicates the contributions of nonadsorbed molecules and free carboxylic-acid ligands during the postannealing of P3HT. These ligands can form H-bonds with the surface. During the postannealing of the TiO_2/P3HT layer in air, the oxygen attacks and is diffused into P3HT. The overall features of this spectrum are similar to those of the Raman spectrum of neutral P3HT, except for the bands at 1010, 1188, 1306, and $1608\ cm^{-1}$. An interesting feature of the Raman spectrum of P3HT is the presence of a band at $1188\ cm^{-1}$, which arises from C_α—$C_{\alpha'}$ inter-ring stretching vibrations of distorted parts of the polymer.[26] The change in the polarizability moment due to distorted C_α—$C_{\alpha'}$ inter-ring stretching is not parallel but at an angle to the thiophene ring.

The bands in the Raman spectrum due to adsorbed carboxylate appear in the range $1150–1600\ cm^{-1}$. Four bands due to carboxylate are likely to be present: C—O stretching (coupled with ring stretches) peaks at $1010\ cm^{-1}$, $1306\ cm^{-1}$, $1379\ cm^{-1}$, and $1608\ cm^{-1}$, which correspond to the Ti—O—C, C—OH (coupled C—O), COO^- symmetric (carboxylate) stretching, and carboxyl group vibration modes, respectively. Carboxy groups can coordinate with metal ions in various ways as follows: physical adsorption via hydrogen bonding, bidentate chemical bonding formation, and bridging. Metal ions can interact with either of the two oxygen atoms of the (COO^-) group.[27] In fact, recent calculations and experiment evidence show that the dissociative adsorption of carboxyl groups at defect sites leads to a much larger redshift in the TiO_2 excitation energy than molecular adsorption. These results are in agreement with those obtained from the absorbance measurements.

Note that the P3HT samples in the three devices were annealed under different conditions. The vibration near $1379\ cm^{-1}$ was assigned to the C_β—$C_{\beta'}$ ring stretching mode and COO^- symmetric stretching. However, no band is evident at $1608\ cm^{-1}$ in Fig. 7(d). Therefore, the comparison of Figs. 7(b) and 7(c) with Fig. 7(d) shows that the Raman spectroscopic changes during the postannealing process result from reactions between P3HT and the oxygen or moisture in the air. We suggest that the $1379\ cm^{-1}$ mode is contributed to by both COO^- symmetric stretching and C_β—$C_{\beta'}$ ring stretching. In contrast to Figs. 7(b) and 7(c), in which bands due to the $1608\ cm^{-1}$ vibration mode are present, the $1608\ cm^{-1}$ vibration mode is not evident in Fig. 7(d), which means that free carboxylic-acid groups are not present. In addition, since a very weak line (C═O, at $1730\ cm^{-1}$) and a strong line (COO^- symmetric stretching, at $1379\ cm^{-1}$) are present, it can be concluded that the attachment of the carboxy groups to TiO_2 occurs via bidentate or bridging bonds. Importantly, two lines (1608 and $1730\ cm^{-1}$) of the Raman spectra appear at precisely the same frequencies in the infrared spectra. The disordered conformational state can be converted to an ordered conformational state by lowering the temperature. This change elongates the conjugation length of the polymer chain and causes a redshift in the optical absorption of P3HT. The decrease in the intensity of the $1445\ cm^{-1}$ band is possibly due to the change in the conformational state of the P3HT layers, because this is the only band associated with the conjugated P3HT segments. However, the formation of surface CT complexes commonly leads to sensitization with respect to visible light. Visible laser Raman spectroscopy is a convenient technique for studying these absorption elements because the laser probe photo-excites the CT complexes, which leads to an enhancement of the Raman scattering phenomenon (resonance Raman scattering, RRS). The P3HT films produce a very strong visible light absorption band with a maximum located at approximately 500 nm, which is related to the $\pi \rightarrow \pi^*$ electronic transition. Therefore, when excited at 514 nm (close to 500 nm), the resonance effect enhances the Raman lines of P3HT.

The FT-Raman spectra in Fig. 8 are not characterized as Raman spectra because they were recorded during laser excitation at 1064 nm; there is no absorption in this region in the UV-vis spectra of P3HT on the TiO_2 and ITO films.

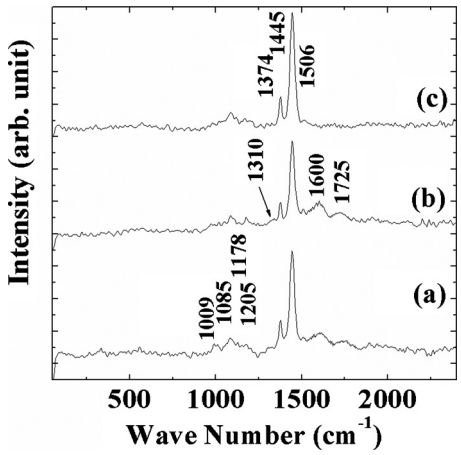

FIG. 8. FT-Raman spectra of the PV cells: (a) with TiO_2 in air; (b) without TiO_2 in N_2; (c) with TiO_2 in N_2.

Many bands in the FT-Raman spectra of P3HT can be correlated with the micro-Raman spectra. The bands at 1009, 1310, 1374, 1600, and 1725 cm^{-1} in the FT-Raman spectra in Fig. 8 that are due to C—O stretching peaks can be correlated with bands appearing at approximately the same positions in the micro-Raman spectra. In particular, the bands at 1600 cm^{-1} in the Raman spectra in Figs. 8(a) and 8(b) are related to those at 1608 cm^{-1} in Figs. 8(b) and 8(c). Thus, the band at 1600 cm^{-1} can be assigned to carboxylic group vibration modes.

Figure 9 shows the FT-IR spectra of the P3HT samples on the TiO_2 and ITO films produced under the various annealing conditions. All of the devices have a broad absorption band between 3700 and 3000 cm^{-1}, which corresponds to the OH bond local vibration modes on the surface of TiO_2. The peak of this band is at approximately 3540 cm^{-1}, which is characteristic of the hydroxyl stretching and bending vibrations of water molecules, and thus indicates the presence of molecularly adsorbed water on the TiO_2 surface. In Fig. 9, strong and clear bonding structures are present at 3178 cm^{-1} and 3670 cm^{-1}, which are associated with hydrogen-bonded O—H and nonhydrogen-bonded O—H vibrations, respectively. More pronounced differences between these spectra are visible in the lines corresponding to the carboxyl groups.

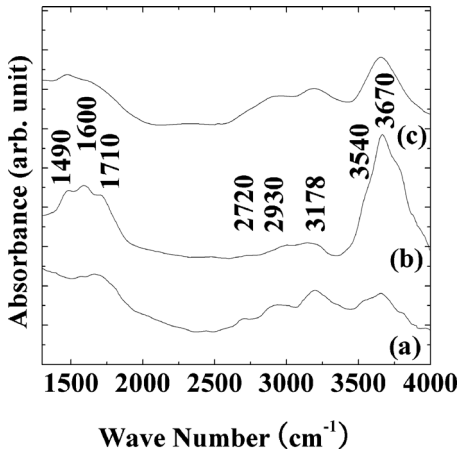

FIG. 9. FT-IR spectra of the PV cells: (a) with TiO_2 in air; (b) without TiO_2 in N_2; (c) with TiO_2 in N_2.

In Figs. 9(a) and 9(b), the absorption bands at approximately 1600 and 1710 cm^{-1} are stronger than those in Fig. 9(c), which can be explained in terms of the contributions of the COO^- asymmetric (carboxylate) stretching mode and the carbon–oxygen double-bond (C═O) respectively. Since the modes of the nonequivalent oxygen are strongly attenuated by postannealing, the carboxylate band dominates the spectrum. These results are in agreement with those obtained from the Raman measurements. The relatively strong band at 1710 cm^{-1} in Figs. 9(a) and 9(b) is associated with the free carboxylic-acid ligands that are created during the postannealing of P3HT, and can be ascribed to the contributions of nonadsorbed molecules or simply to the signal of nonbound carboxyl groups. In contrast to the FT-Raman and micro-Raman results, the FT-IR results do not indicate the frequencies of the stretching modes of the carboxyl groups in the ionic states. However, the evidence for a weak (C═O) stretching mode and the carboxylate stretching modes strongly support the idea that adsorption occurs via bridging or bidentate linkages. In Fig. 9(a), a weak band assigned to carbon atoms bonded to hydrogen atoms and double-bonded to oxygen atoms (chemical formula O═CH—) is present at 2720 cm^{-1}. If an alkyl-substituted thiophene thin film is sufficiently ordered and oriented, the extent of side-chain interdigitation can be determined from the lamellar spacing, the side-chain length, and the side-chain tilt away from the lamella normal.[13] No single measurement can determine the degree of interdigitation, so we used XRD to measure the lamellar spacing and polarized FT-IR to measure the side-chain tilt. Polarized FT-IR can be used to determine the tilt angles of the mutually orthogonal transition dipole moments for the methylene symmetric and antisymmetric stretches. Polarized IR can also be used to determine the level of local structural order of the alkane chains by examining the frequency of the methylene antisymmetric stretch. Values near 2918 cm^{-1} indicate the presence of highly ordered and all-trans alkane chains, whereas values near 2928 cm^{-1} indicate the presence of liquid-like alkane chains.[28] The methylene antisymmetric stretch locations for P3HT are near 2930 cm^{-1}. Therefore, the hexyl chains of P3HT are liquid-like and highly disordered.[29]

In conventional semiconductor physics, the HOMO and lowest unoccupied molecular orbital (LUMO) levels can be treated as the valence band (VB) and conduction band (CB), respectively. First, PL excitation (PLE) spectroscopy was used to find the wavelength of the strongest excitation that could be considered an absorption peak of the films. We then determined the excitation wavelength of pure P3HT and the hybrid films at 488 nm. TiO_2 does not absorb in the visible light range. Note also that the electronic transitions are slightly affected by the absorption. The absorption shifts to lower energies when complexes are attached to the semiconductor surface, in particular for P3HT. These shifts can be interpreted as the result of an appreciable interaction between P3HT and the TiO_2 film, which is very important for the efficiency of solar cells.

Figure 10 shows the PL spectra of TiO_2 layers excited by UV light at 325 nm at room temperature. PL bands for the TiO_2 layers are present, including six main Gaussian-type

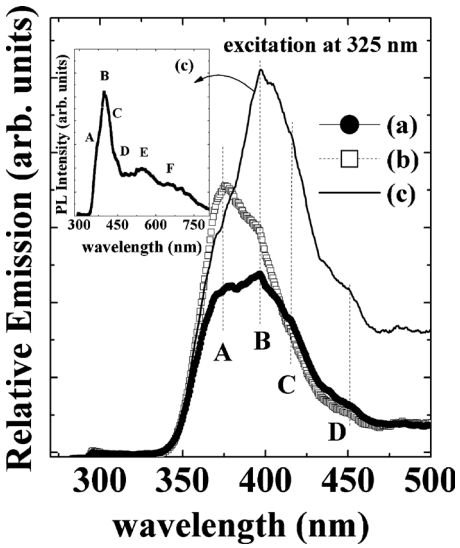

FIG. 10. Normalized PL spectra of the TiO_2 emission areas in the PV cells obtained by using He—Ne laser excitation at 325 nm: (a) with TiO_2 in N_2; (b) with TiO_2 in air; and (c) pure TiO_2.

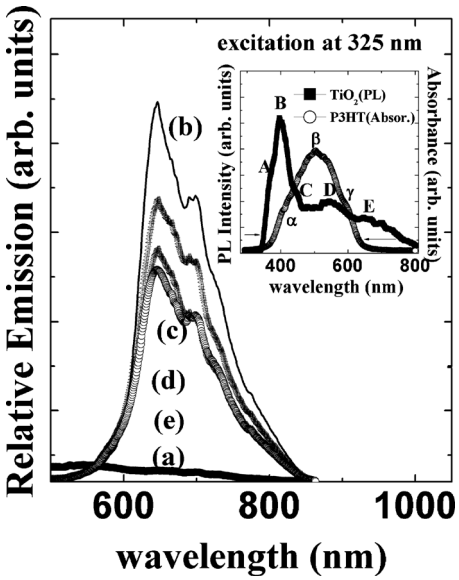

FIG. 11. Normalized PL spectra of the P3HT emission areas in PV cells obtained by using He—Ne laser excitation at 325 nm: (a) pure TiO_2; (b) with TiO_2 in N_2; (c) without TiO_2 in N_2; (d) with TiO_2 in air; (e) P3HT. The upper inset shows the absorption spectra (open circles) for P3HT and the PL spectra (closed squares) for TiO_2. The closed square emission curve was excited at 488 nm.

peaks at 370 nm, 397 nm, 419 nm, 450 nm, 541 nm, and 660 nm (shown in Fig. 10 and in the inset in Fig. 10) denoted A, B, C, D, E, and F, respectively. The emission bands around 370 nm are assigned to direct recombination from the CB to the VB, and vary only slightly between the different interfaces and TiO_2 surfaces. The presence of the emission band at 397 nm reflects the surface status, and in particular the incomplete surface passivation. When compared to the peak near 370 nm due to the TiO_2 surface [see Fig. 10(c)], the TiO_2 interface [see Fig. 10(b)] is clear but the peak at 397 nm due to the TiO_2 interface is feeble, which shows that the interface states have been destroyed, especially the Ti—OH states. UV light can easily change the TiO_2 surface electronic structure. Most of the TiO_2 is destroyed and slowly replaced by Ti—OH, as has been confirmed by photoinduced super hydrophilicity studies, so the capture of photoinduced electrons by TiO_2 decreases accordingly and the intensity of the peak at 397 nm decreases. It is expected that indirect recombination will stem from surface recombination via oxygen vacancies. PL peaks are present at 419 and 450 nm in Figs. 10(a) and 10(c) but these peaks are not present in (b). Some authors have attributed this flat band to the trapping of excitonic PL peaks by surface states and defects; this band is also easily affected by factors related to the surface. The peak at 419 nm is due to the trapping of excitonic PL peaks by surface states. Bulk impurities arise mainly in the form of oxygen defects and can act as the centers of indirect recombination, so the peak at 450 nm is thought to be due to indirect recombination via oxygen defects.[30,31] In the inset in Fig. 10, the broad emission band at 541 nm is composed of two Gaussian-type bands. These bands are attributed to the radiative recombination of surface oxygen vacancies and self-trapped excitons.[32] It is expected that annealing at high temperatures will break the binding between oxygen and titanium in the TiO_2 films and then pull oxygen out of the sample. The broad luminescence band centered at 660 nm is associated with the recombination of electrons from the CB edge with holes trapped at interstitial Ti^{3+} sites.[33] In particular, there is a significant quenching of PL in the layered sample as compared with that found in pure TiO_2. The PL quenching in the TiO_2/P3HT bilayer film might be due to following two different effects: (i) photoinduced back CT and (ii) resonance energy transfer between energy species in the excited state, due to the overlap between the emission and absorption spectra. Such resonance energy transfer depends on the intermolecular distance and the spectral overlap as well as on the mutual transition dipole orientation. For CT to occur, the binding energy of the photogenerated exciton should be smaller than the difference between the electron affinities of the participating donor and acceptor materials, when corrected for the Coulomb attraction between the separated charges. In addition, the yield of the PL emission in the bilayer decreases substantially in the presence of TiO_2. This decreased PL intensity indicates that charge separation occurs at the interface between the two materials. This separation produces a charge-separated state consisting of an electron on the TiO_2 and a hole on the polymer, which is responsible for the TiO_2 emission quenching.

Figure 11 shows plots of the PL spectra obtained for the P3HT samples by using a spectrometer with an He—Ne laser excitation source (λ=325 nm). It can be seen that all the samples produce broad photoemissions with following two peaks: one at 645 nm and the other at 690 nm. The TiO_2/P3HT bilayer produces two electroluminescence peaks, at 580 and 640 nm; the first peak is more intense than the second. The negligible differences in the position and intensity of these emission peaks can be explained in terms of electroluminescence. In Fig. 11, it can be seen that the photoemissions of the hybrid samples exhibit higher luminescence intensity than that of pure P3HT. However, the strongest PL enhancement arises for (b) TiO_2/P3HT (in N_2),

whereas the PL intensities for (c) P3HT (in N_2) and (d) TiO_2/P3HT (in air) did not increase significantly. In these hybrid films, no blueshift was obtained; blueshifts would be explained by a reduction in the polymer conjugation chain length. Although PL enhancement in these systems has rarely been discussed, one suggestion is that the increased PL intensity of such P3HT layers can be explained in terms of the large absorption coefficient of TiO_2. This interpretation can be seen for instance in Ref. 34, where the authors recently discussed PL enhancement in TiO_2/P3HT. This phenomenon was explained as due to nonradiative FRET (Ref. 9) from TiO_2 to the polymer for excitation at wavelengths of less 350 nm. The inset in Fig. 10 shows the region of overlap between the UV-visible absorption of P3HT and the PL spectrum of TiO_2. It can be obvious that the overlapping results could be possibly transferred between TiO_2 and P3HT by means of FRET. FRET is mediated by dipole–dipole interactions, the strength of which critically depends on among other influences the spectral overlap between donor (TiO_2) emission and acceptor (P3HT) absorption and on the dipole separation distance.[9,35] Energy alignment is thus needed in order to maximize the resonant coupling between the inorganic and organic excitations.[36] In Fig. 11, expansion of the 550–850 nm region shows that the intensity of P3HT emissions arising from excitation of TiO_2/P3HT at 325 nm is greater than that arising from excitation of P3HT at 325 nm. Thus the majority of emissions from TiO_2 upon He—Ne laser excitation can be attributed to absorption and FRET from the absorbing P3HT. Since the inorganic material and the polymer have different emission and absorption spectra with some overlap, the energy could possibly be transferred between the two components by means of FRET (Refs. 9 and 37) and photon recycling effects.[38] FRET is a near-field long range energy transfer process that enables excitons to transfer between molecules for distances above 25 nm.[39] In the hybrid device, it is possible for P3HT (donors) to transfer excitons to neighboring TiO_2 (acceptors) close to the donor/acceptor interface, because a part of the absorption spectrum overlaps with the P3HT emission spectrum.

The inset in Fig. 12 shows the room-temperature UV-visible absorption and PL spectra of TiO_2 and P3HT, respectively. P3HT produces a broad recombination spectrum with a peak at approximately 600 nm and the spectrum of TiO_2 contains a sharp absorption edge at approximately 350 nm. There are no additional absorption peaks in the measured spectral range. The degree of PL quenching can also provide information about the quality of the interconnection of TiO_2 and the polymer and the nature of their interface. In Fig. 12, for excitation at 488 nm only the polymer is excited; the PL spectra of the devices contain similar emission features to that of pure P3HT, which indicates that the luminescence predominantly results from excitons that radiatively recombine in the polymer. However, the yield of the PL emission in the composites decreases substantially in the presence of TiO_2. This decreased PL intensity indicates that charge separation occurs at the interface between the two materials. i.e., a charge-separated state with an electron on the TiO_2 and a hole on the polymer is responsible for the polymer emission quenching. PL quenching provides direct evidence for exciton dissociation; efficient PL quenching is necessary to obtain efficient organic solar cells. However, this does not necessarily mean that the stronger the PL quenching, the better the performance of the solar cells. Similar observations have also been reported for poly(3-octylthiophene), which consists of thiophene rings with large alkyl groups,[40] and for MEHP-PPV/CdSe-nanoparticle composite films.[41] Rapid charge separation at the TiO_2/P3HT interface leads to efficient exciton dissociation, and thus results in quenching of the PL efficiency. Thus, the PL quenching results in Figs. 11 and 12 indicate the occurrence of photon-mediated electronic transitions (FRET) and photoinduced CT, respectively.

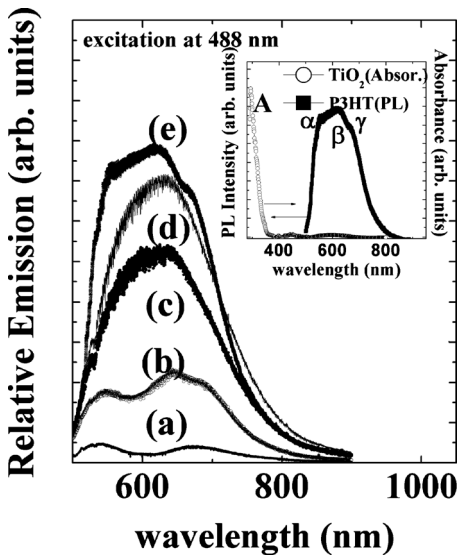

FIG. 12. Normalized PL spectra of the P3HT emission areas in PV cells obtained by using Ar laser excitation at 488 nm: (a) pure TiO_2; (b) with TiO_2 in N_2; (c) without TiO_2 in N_2; (d) with TiO_2 in air; (e) P3HT. The upper inset shows the absorption spectra (open circles) for TiO_2 and the PL spectra (closed squares) for P3HT. The closed square emission curve was excited at 488 nm.

In this study, all samples were tested at a constant film thickness to compare the optical absorption and PL intensities of P3HT and TiO_2. Figure 13 shows the UV-vis spectra of the polymer films. In a conjugated polymer, the extent of conjugation directly affects the observed energy of the $\pi-\pi^*$ transition, which appears as the maximum absorption (λ_{max}) in its UV-vis spectrum. The spectrum of P3HT contains a peak at 520 nm and two shoulders at 560 and 612 nm, which are attributed to its crystalline π-stacking structure. The red-shifted absorption of P3HT is due to the better chain packing induced by three-dimensional ordering of the polymer chain,[42] which increases the average length and decreases the HOMO–LUMO band gap.[43] P3HT in (c) and (d) has a lower absorbance than P3HT in (b) and (e), and the λ_{max} of P3HT in (c) and (d) is 10 nm blueshifted (from 510 to 500 nm) with respect to that of P3HT in (b) and (e). This result can be explained in terms of a change in the stacking conformation of the polymer structure from high crystallinity to lower crystallinity, and a reduction in the intraplane and interplane stacking, which causes a poor $\pi-\pi^*$ stacking transition and lower absorbance. However, contrary to the peak at 350 nm [in Fig. 13(d)], the slop at 310 nm [in Fig. 13(e)] do not show any change with pure TiO_2 [in Fig. 13(a)]. The inves-

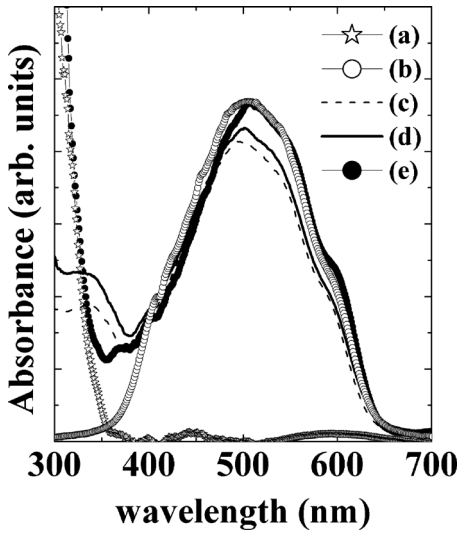

FIG. 13. Normalized UV-vis absorption spectra of films and PV cells: (a) pure TiO_2; (b) P3HT; (c) without TiO_2 in N_2; (d) with TiO_2 in air; (e) with TiO_2 in N_2.

tigated carboxy ligands were found to undergo unique binding at the surface, resulting in new hybrid properties of the surface modified materials. These hybrid properties arise from the ligand-to-metal localized CT interaction between the ligand and surface metal atoms. The results in Fig. 13(e) can be explained in terms of the interaction between TiO_2 and the P3HT surface, which arises through carboxylate attachment via bidentate or bridging coordination to the TiO_2 surface. Note, that these results are remarkably consistent with the micro-Raman and FT-IR results.

Figure 14 shows a schematic representation of the energy levels and the coupled transitions involved in TiO_2 emission and P3HT absorption in FRET. Process (1) is the photoexcitation of both the electron donor (P3HT) and the electron acceptor (TiO_2); charge separation at the interface between P3HT and TiO_2 results due to the dissociation of excitons. From the PL quenching measurements, it can be

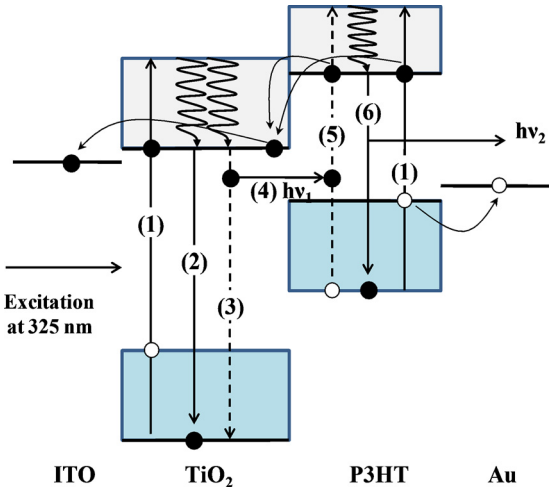

FIG. 14. (Color online) Schematic representation of the energy levels and the coupled transitions involved in TiO_2 emission and P3HT absorption in fluorescence resonance energy transfer: (1) absorption (excitation); (2) fluorescence emission; (3) resonance energy transfer; (4) nonradiative energy transfer; (5) nonradiative excitation; (6) sensitized emission.

concluded that this process occurs in this device. Dissociation of bound electron–hole pairs (excitons) by diffusional motion results in the formation of free mobile holes in P3HT, which leads to the observed higher photocurrent. However, both TiO_2 and P3HT absorb photons upon excitation at 325 nm. Note that each of the two materials play the roles of both donor and acceptor. In FRET, (1) absorption (excitation) and (2) emission transitions are represented by straight vertical arrows, and vibrational relaxation is indicated by wavy arrows. The coupled transitions [(3) nonradiative energy transfer and (5) nonradiative excitation] are drawn as dashed lines to suggest their correct placement in the diagram if they had arisen from photon-mediated electronic transitions [(4) resonance energy transfer]. In the presence of a suitable acceptor (P3HT), the donor (TiO_2) can transfer excited state energy directly to the acceptor (P3HT) without emitting a photon [express donor (TiO_2) energy transfer (4) as $h\nu_1$]. The resulting sensitized fluorescence emission has characteristics similar to the emission spectrum of the acceptor (P3HT). FRET is a process by which radiationless transfer of energy occurs from an excited state donor (TiO_2) to a second acceptor (P3HT) in close proximity. The range over which the energy transfer can take place is limited to approximately 10 nm, i.e., the efficiency of transfer is extremely sensitive to the distance between the donor (TiO_2) and the acceptor (P3HT). FRET involves a donor (TiO_2) in an excited electronic state, which may transfer its excitation energy to a nearby acceptor (P3HT) in a nonradiative fashion through long range dipole–dipole interactions. In FRET, the excited donor (TiO_2) is an oscillating dipole that can undergo an energy exchange with a second dipole with a similar resonance energy (coupled energy). In contrast, radiative energy transfer requires the emission and reabsorption of a photon and depends on the physical dimensions and optical properties of the material, as well as on the geometry of the container and the wavefront pathways. Unlike radiative mechanisms, the study of FRET can yield a significant amount of structural information about the donor–acceptor pair. In addition to the overlapping emission and absorption spectra of the donor and acceptor (see the inset in Fig. 11), the two materials involved in FRET must be positioned within a range of 1–10 nm of each other.

IV. CONCLUSIONS

In conclusion, the device performances and films of organic–inorganic hybrid PV cells containing TiO_2 and P3HT have been characterized for various P3HT postannealing conditions. The performances of the devices postannealed in a N_2 atmosphere (0.11%) were found to be superior to those postannealed in air (0.02%). For the P3HT film annealed under a N_2 atmosphere, the results of HRGIXD and the pole figure show that the backbones of P3HT are aligned with their long axes parallel to the azimuthal TiO_2 and ITO direction, the conjugated planes are slightly tilted, and the side chains are substantially tilted. The results of micro-Raman, FT-IR, and FT-Raman demonstrate that the carboxylate groups attach via bidentate or bridging coordination to the TiO_2 surface, which leads to photoinduced CT processes between TiO_2 and P3HT. The emission region of the PL

spectra of P3HT indicates large quenching (with excitation at 488 nm) and enhanced emission (with excitation at 325 nm). Note that each of the two materials play the roles of both donor and acceptor. All these results can be correlated with the I-V characteristics of the hybrid devices in order to interpret the enhanced efficiencies. Our study of the effects of the postannealing of the polymer has revealed the occurrence of resonance energy transfer at the interface between TiO_2 and P3HT, which indicates that the efficiency of hybrid PV cells can be enhanced by FRET due to overlap between the emission and absorption spectra.

ACKNOWLEDGMENTS

This research was supported by Samsung Electronics Co. Ltd. and the Korea Research Foundation Grant funded by the Korean Government (MOEHRD) (Grant No. KRF-2008-005-J04104).

[1]K. M. Coakley and M. D. McGehee, Chem. Mater. **16**, 4533 (2004).
[2]K. M. Coakley and M. D. McGehee, Appl. Phys. Lett. **83**, 3380 (2003).
[3]A. C. Arango, L. R. Johnson, V. N. Bliznyuk, Z. Schlesinger, S. A. Carter, and H. H. Horhold, Adv. Mater. **12**, 1689 (2000).
[4]T. J. Savenije, J. M. Warman, and A. Goossens, Chem. Phys. Lett. **287**, 148 (1998).
[5]P. A. van Hal, M. P. T. Christiaans, M. M. Woenk, J. M. Kroon, and R. A. J. Janssen, J. Phys. Chem. B **103**, 4352 (1999).
[6]L. H. Slooff, M. M. Wienk, and J. M. Kroon, Thin Solid Films **451–452**, 634 (2004).
[7]P. Ravirajan, S. A. Haque, D. Poplavskyy, J. R. Durrant, D. D. C. Bradley, and J. Nelson, Thin Solid Films **451–452**, 624 (2004).
[8]T. Förster, Ann. Phys. **2**, 55 (1948).
[9]T. Förster, Discuss. Faraday Soc. **27**, 7 (1959).
[10]S. Blumstengel, S. Sadofev, C. Xu, J. Puls, and F. Henneberger, Phys. Rev. Lett. **97**, 237401 (2006).
[11]G. Itskos, G. Heliotis, P. G. Lagoudakis, J. Lupton, N. P. Barradas, E. Alves, S. Pereira, I. M. Watson, M. D. Dawson, J. Feldmann, R. Murray, and D. D. C. Bradley, Phys. Rev. B **76**, 035344 (2007).
[12]Y. R. Park and K. J. Kim, Thin Solid Films **484**, 34 (2005).
[13]D. M. DeLongchamp, R. J. Kline, E. K. Lin, D. A. Fischer, L. J. Richter, L. A. Lucas, M. Heeney, I. McCulloch, and J. E. Northrup, Adv. Mater. **19**, 833 (2007).
[14]G. W. Heffner and D. S. Pearson, Macromolecules **24**, 6295 (1991).
[15]R. A. Street, J. E. Northrup, and A. Salleo, Phys. Rev. B **71**, 165202 (2005).
[16]T. J. Prosa, M. J. Winokur, and R. D. McCullough, Macromolecules **29**, 3654 (1996).
[17]Z. Bao, A. Dodabalapur, and A. J. Lovinger, Appl. Phys. Lett. **69**, 4108 (1996).
[18]H. Sirringhaus, P. J. Brown, R. H. Friend, M. M. Nielsen, K. Bechgaard, B. M. W. Langeveld-Voss, A. J. H. Spiering, R. A. J. Janssen, E. W. Meijer, P. Herwig, and D. M. de Leeuw, Nature (London) **401**, 685 (1999).
[19]R. Azumi, E. Mena-Osteritz, R. Boese, J. Benet-Buchholz, and P. Bauerle, J. Mater. Chem. **16**, 728 (2006).
[20]B. Grévin, P. Rannou, R. Payerne, A. Pron, and J. P. Travers, Adv. Mater. **15**, 881 (2003).
[21]R. J. Kline, M. D. McGehee, E. N. Kadnaikova, J. Liu, and M. J. Frechet, Adv. Mater. **15**, 1519 (2003).
[22]P. P. Lottici, D. Bersani, M. Braghini, and A. Montenero, J. Mater. Sci. **28**, 177 (1993).
[23]V. Swamy, A. Kuznetsov, L. S. Dubrovinsky, R. A. Caruso, D. G. Shchukin, and B. C. Muddle, Phys. Rev. B **71**, 184302 (2005).
[24]F. Chen, G. Shi, J. Zhang, and M. Fu, Thin Solid Films **424**, 283 (2003).
[25]U. Betz, M. Kharrazi Olsson, J. Marthy, M. F. Escolá, and F. Atamny, Surf. Coat. Technol. **200**, 5751 (2006).
[26]E. A. Bazzaoui, G. Levi, S. Aeiyach, J. Aubard, J. P. Marsault, and P. C. Lacaze, J. Phys. Chem. **99**, 6628 (1995).
[27]G. B. Deacon and R. J. Philips, Coord. Chem. Rev. **33**, 227 (1980).
[28]M. C. Gurau, D. M. Delongchamp, B. M. Vogel, E. K. Lin, D. A. Fischer, S. Sambasivan, and L. J. Richter, Langmuir **23**, 834 (2007).
[29]R. A. MacPhail, H. L. Strauss, R. G. Snyder, and C. A. Elliger, J. Phys. Chem. **88**, 334 (1984).
[30]J. Liqiang, Q. Yichuna, W. Baiqia, L. Shudana, J. Baojianga, Y. Libina, F. Weia, F. Hongganga, and S. Jiazhongb, Sol. Energy Mater. Sol. Cells **90**, 1773 (2006).
[31]B. S. Liu, X. J. Zhao, and L. P. Wen, Mater. Sci. Eng., B **134**, 27 (2006).
[32]H. Tang, H. Berger, P. E. Schmid, and F. Levy, Solid State Commun. **87**, 847 (1993).
[33]R. Sanjinés, H. Tang, H. Berger, F. Gozzo, G. Margaritondo, and F. Lévy, J. Appl. Phys. **75**, 2945 (1994).
[34]Y. T. Lin, T. W. Zeng, W. Lai, C. W. Chen, Y. Y. Lin, Y. S. Chang, and W. F. Su, Nanotechnology **17**, 5781 (2006).
[35]T. Virgili, D. G. Lidzey, and D. D. C. Bradley, Adv. Mater. **12**, 58 (2000).
[36]D. Basko, G. C. LaRocca, F. Bassani, and V. M. Agranovich, Eur. Phys. J. B **8**, 353 (1999).
[37]Y. Liu, M. A. Summers, C. Edder, J. M. J. Fréchet, and M. D. McGhee, Adv. Mater. **17**, 2960 (2005).
[38]Y. Liu, M. A. Summers, S. R. Scully, and M. D. McGehee, J. Appl. Phys. **99**, 093521 (2006).
[39]A. Martí, L. Cyadra, and A. Luque, Physica E **14**, 150 (2002).
[40]A. Watanabe, T. Kodaira, and O. Ito, Chem. Phys. Lett. **273**, 227 (1997).
[41]Y. Y. Lin, C. W. Chen, J. Chang, T. Y. Lin, I. S. Liu, and W. F. Su, Nanotechnology **17**, 1260 (2006).
[42]Y. Kim, S. Cook, S. M. Tuladhar, S. A. Choulis, J. Nelson, J. R. Durrant, D. D. C. Bradley, M. Giles, I. McCulloch, C. S. Ha, and M. Ree, Nature Mater. **5**, 197 (2006).
[43]P. J. Brown, D. S. Thomas, A. Köhler, J. S. Wilson, J. S. Kim, C. M. Ramsdale, H. Sirringhaus, and R. H. Friend, Phys. Rev. B **67**, 064203 (2003).